UV-Vis Spectroscopy for Characterization of Metal Nanoparticles Formed from Reduction of Metal Ions During Ultrasonic Irradiation

4

Kenji Okitsu

Contents

1   Overview

The reduction processes of metal ions can be used to prepare metal nanoparticles in an aqueous solution, in which UV-Vis spectroscopy can be used as an excellent tool to characterize the properties of metal nanoparticles, in particular the size and shape of the metal nanoparticles and their surface property in the state of the colloidal dispersion system. In addition, UV-Vis spectroscopy enables the amount of precursor metal ions used during the formation of metal nanoparticles to be measured. In this chapter, the sonochemical reduction processes for Pd(II), Au(III), Pt(II), Pt(IV), Ag(I), and MnO_4^- are described on the basis of changes in the absorption
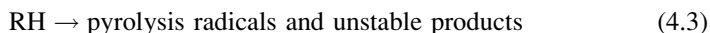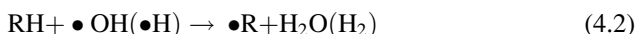
K. Okitsu
Graduate School of Engineering, Osaka Prefecture University, Naka-ku, Sakai, Osaka, Japan

spectrum during ultrasonic irradiation to understand the sonochemical reduction mechanism of metal ions. In addition, the optical properties of the sonochemically formed metal nanoparticles such as the spherical nanoparticles of Pd, Au, Pt, Ag, MnO_2, and Au/Pd and the shape-controlled nanoparticles are reviewed to understand the formation processes during ultrasonic irradiation.

2   Introduction

Metal nanoparticles have attracted considerable attention in various fields of technology because of their useful physicochemical properties arising from the effects of the size of nanoparticles. The structure and shape of the nanoparticles are also important factors to control their properties. Therefore, various types of preparation methods such as controlled chemical methods with an appropriate reductant [1–4] as well as photochemical and radiation chemical methods [5, 6] have been actively developed. Although there are a number of methods available to prepare metal nanoparticles, a sonochemical method offers unique synthetic processes: the sonochemical method involves radical reactions and/or thermal reactions, which originate from extremely high temperatures and pressures generated in cavitation bubbles. In addition, strong shock waves and micro-jet flows are also induced by ultrasonic irradiation of a liquid as a consequence of a cavitation phenomenon.

The reduction processes can be conveniently used to prepare metal nanoparticles in an aqueous solution. As representative reactions, the following reactions proceed under ultrasonic irradiation in an aqueous solution containing an organic additive (RH) under a rare gas atmosphere [7]:

$$H_2O \rightarrow \bullet OH + \bullet H \tag{4.1}$$

$$RH + \bullet OH(\bullet H) \rightarrow \bullet R + H_2O(H_2) \tag{4.2}$$

$$RH \rightarrow \text{pyrolysis radicals and unstable products} \tag{4.3}$$

$$M^{n+} + \text{reductants} \rightarrow M^0 \tag{4.4}$$

$$nM^0 \rightarrow \left(M^0\right)_n \tag{4.5}$$

$$M^0 + \left(M^0\right)_n \rightarrow \left(M^0\right)_{n+1} \tag{4.6}$$

where M^{n+} and M^0 correspond to a metal ion and metal atom, respectively. Reactions (4.1)–(4.3) indicate the sonochemical formation of reductants: (4.1) •H is formed from the pyrolysis of water, (4.2) •R and H_2 are formed from the abstraction reaction of RH with •OH or •H, and (4.3) pyrolysis radicals and unstable products are formed via the pyrolysis of RH. Some of the pyrolysis radicals and unstable products act as reductants. In this mechanism, most of the organic

additives used, including general organic stabilizers such as surfactants or water-soluble polymers, correspond to RH. After the formation of M^0, some of the M^0 aggregate to form small particles, $(M^0)_n$, as Eqs. 4.4 and 4.5. In addition to such aggregation, the formed M^0 can be adsorbed on $(M^0)_n$ to give $(M^0)_{n+1}$, as Eq. 4.6. The general mechanisms for the formation of metal nanoparticles are studied elsewhere [1–4].

Sonochemical reduction processes can be used as eco-friendly techniques for the synthesis of nanoparticles, because these experiments can be conducted in a solution at around room temperature and the amounts of used reagents and/or reaction times can be reduced [7–10]. Since the sonochemical processes offer unique synthetic routes, they are expected to be promising ones to synthesize various types of novel functional nanoparticles.

Although there are some reviews about the sonochemical synthesis of metal nanoparticles, the UV-Vis spectrum analyses for the formation of the metal nanoparticles as well as the reduction of metal ions are not described comprehensively. Therefore, in this chapter, the comprehensive data for changes in the absorption spectrum of the sample solution during ultrasonic irradiation are shown and analyzed to understand the mechanism for the formation of metal nanoparticles and reduction of metal ions, where the synthesis of spherical metal nanoparticles of Pd, Au, Pt, Ag, MnO_2, and Au/Pd and the synthesis of shape-controlled nanoparticles of Au nanorods are described.

3   Experimental and Instrumental Methodology

Various types of sonicators and irradiation systems have been used for sonochemical reactions. An ultrasonic cleaning bath can be used conveniently; however, when the intensity of ultrasound is not high enough, the sonochemical reactions with OH or H radicals do not occur sufficiently. This is because hot cavitation bubbles do not generate sufficiently and thus the amounts of OH or H radicals formed are very small. On the other hand, a horn-type sonicator can be used as a high-intensity sonicator, which is often used as a strong homogenizer. Although a horn-type sonicator can produce hot cavitation bubbles, the frequency of ultrasound is generally limited to as low as 20–50 kHz. Stronger physical effects such as shock waves and micro-jet flows are also induced by the irradiation with a lower frequency sonicator. This is because changes in the size of the cavitation bubbles during ultrasonic irradiation are larger at the lower frequency.

In this chapter, a standing-wave-type irradiation system is mainly used for the sonochemical reduction of metal ions and formation of metal nanoparticles. The representative irradiation setup and the characteristics of the reaction vessel are shown in Fig. 4.1 [11]. In this system, standing waves are formed by overlapping the irradiated ultrasound with the ultrasound reflected at the top interface of the sample solution. The glass vessel is cylindrical and it has a Teflon valve and a port covered by a silicon septum for gas bubbling. The bottom of the vessel is planar, 1 mm thick and 55 mm in diameter. The vessel is mounted at a fixed position. Since

Fig. 4.1 One example of the irradiation setup and the characteristic of the reaction vessel in a standing-wave-type irradiation system (Reprinted with permission from Ref [11]. Copyright 2002 The Chemical Society of Japan)
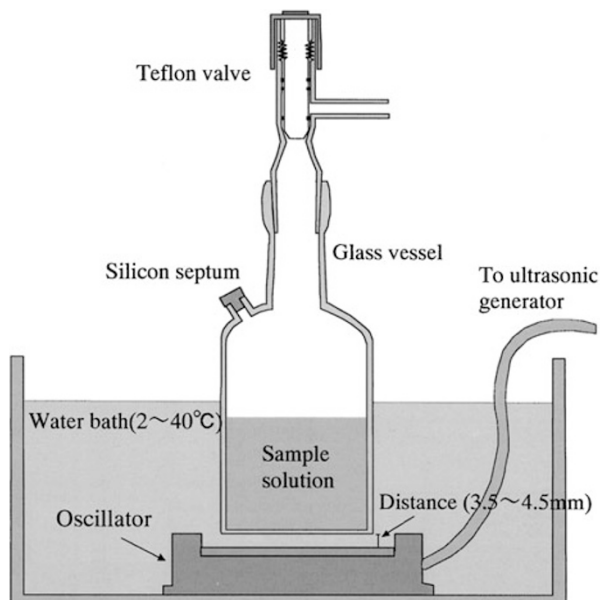
the distance from the oscillator to the vessel bottom affects sonochemical efficiency [11], the distance from the oscillator must be controlled carefully. In general, the vessel bottom is fixed at the $\lambda/2$ distance from the oscillator to get high sonochemical efficiency, where λ is the wavelength of ultrasound in the sample solution.

As a sample solution, an aqueous solution of metal ions (e.g., 0.1–1.0 mM, 60 or 65 mL) is added to the vessel. Since a dissolved gas in the sample solution strongly affects sonochemical efficiency [11, 12], the solution should be purged with an appropriate gas. After purging, ultrasonic irradiation is carried out using an ultra-sonic generator (4,021type; frequency, 200 kHz; Kaijo Co.) and a 65 mmϕ oscil-lator (Kaijo Co.), which is operated at ca. 20–200 W in a water bath maintained at a constant temperature. In this chapter, figures other than Fig. 4.11 are based on the results obtained by this irradiation system. After irradiation, small amounts of the sample solutions are drawn from the silicon septum by a syringe with a stainless-steel needle and then the sample solutions are analyzed by UV-Vis spectroscopy and/or various analytical methods.

As described in the reduction mechanism, organic compounds, which act as a precursor for the formation of reductants during ultrasonic irradiation, are added before or after gas purging. When a high-volatile organic compound is added to the sample solution, its vaporization property should be considered: the addition of a high-volatile compound should be performed after gas purging to avoid the decrease in the concentration by its vaporization.

As a matter of course, the physicochemical properties of the cavitation bubbles affect the reduction processes of the metal ions as well as various chemical reactions. Since the bubble temperature is one of the most important factors to

control the chemical effects of cavitation, it is important to understand the bubble temperature of the used irradiation system. To estimate the bubble temperature, analyses of sonoluminescence (light emission from a cavitation bubble) and reaction kinetics can be used. Here, we briefly present the analysis of reaction kinetics. Based on the literature [12–15], the bubble temperature can be estimated from the sonolysis of a *tert*-butyl alcohol (*t*-BuOH) aqueous solution in the presence of an appropriate rare gas. During the sonolysis of this solution, CH_3 radicals are formed by the pyrolysis of *t*-BuOH, which then react to form C_2H_2, C_2H_4, and C_2H_6. Since the product ratio $(C_2H_2 + C_2H_4)/C_2H_6$ is dependent on the temperature, the bubble temperature can be estimated by analyzing the yield of these products: the product ratio is equal to the ratio k_2/k_1, where k_1 (rate constant for $2CH_3 \rightarrow C_2H_6$) is $2.4 \times 10^{14}\, T^{-0.4}\, dm^3\, mol^{-1}\, s^{-1}$ and k_2 (rate constant for $2CH_3 \rightarrow C_2H_4 + H_2$) is $1.0 \times 10^{16} \exp(-134\, kJ/RT)\, dm^3\, mol^{-1}\, s^{-1}$. C_2H_2 is formed via the thermal reaction of C_2H_4.

Figure 4.2 shows the estimated bubble temperature as a function of the thermal conductivity of each rare gas [12]. It can be seen that the bubble temperature is about 3,900 K and is almost the same among all of the rare gases. In the analysis of sonoluminescence induced by using a horn-type 20-kHz sonicator, the bubble temperatures decrease with increasing thermal conductivity of the dissolved gases, where it is considered that the greater the conductivity of the gas, the more heat is dissipated to the surroundings, resulting in the decrease in the bubble temperature. Until now, the bubble temperatures estimated from analyses of the sonoluminescence, reaction kinetics, and a computer simulation are generally in the range between 3,900 and 30,000 K [12–21].

In addition to the measurement of the bubble temperature, chemical efficiency is often measured. The yield of H_2O_2 formed in the sonolysis of pure water can be regarded as the chemical efficiency [11, 22], because the yield of H_2O_2 can be connected to that of the OH primary radicals formed in the sonolysis of water.

$$2 \bullet OH \rightarrow H_2O_2 \tag{4.7}$$

Koda et al. [22] investigated the effect of frequency on the sonochemical efficiency in the frequency range of 19.5–1.2 MHz, where the yields of H_2O_2 were measured by KI oxidation and the Fricke reaction (Fe(II) oxidation) with a UV-Vis spectrophotometer. They showed that the highest chemical efficiency existed in the range of 96–500 kHz. In addition, the liquid height of the sample solution also affects the sonochemical efficiency [23]. Therefore, to get high chemical efficiency, the frequency and liquid height should be optimized as well as the configuration of the irradiation system.

As a reference, we introduce several examples for the effects of frequency on the chemical reactions. From the viewpoint of environmental remediation, the degradation of 1,4-dioxane and CCl_4 has been investigated. In the case of 1,4-dioxane, the rate of degradation was the highest at 358 kHz in the frequency range of 205–1,071 kHz [24]. In the case of CCl_4, the rate of degradation was the highest at around 500–618 kHz in the frequency range of 20–1,078 kHz [25]. On the other

Fig. 4.2 Cavitation bubble temperature estimated in the presence of different rare gases from the analysis of reaction kinetics. Ultrasound (200 kHz) is irradiated to a *t*-BuOH aqueous solution at 20 °C (Reprinted with permission from Ref. [12]. Copyright 2006 American Chemical Society)
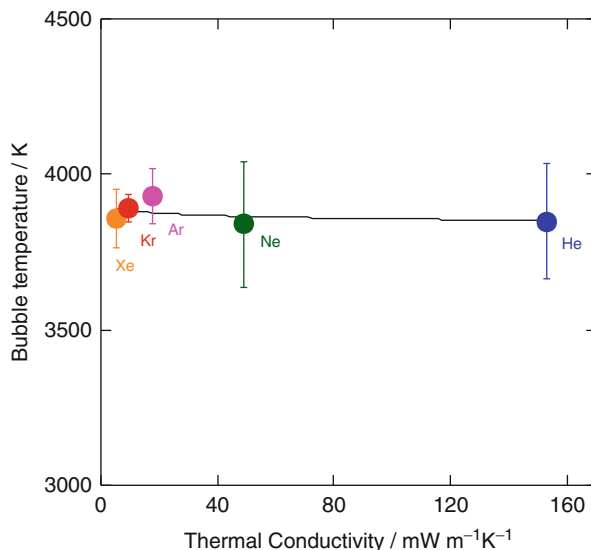
hand, from the viewpoint of the reduction of metal ions to form metal nanoparticles, the effect of frequency on the rate of reduction has been investigated. For example, the rate of Au^{3+} reduction in the presence of 1-propanol decreased with increasing frequency (213 kHz > 358 kHz > 647 kHz > 1062 kHz), and the rate was the lowest when a horn-type sonicator of frequency 20 kHz was used [26]. Here, UV-Vis spectroscopy acts as a strong tool for the measurement of the concentration of Au^{3+} in an aqueous solution during ultrasonic irradiation.

In the following section, the formation of metal nanoparticles is described in connection with the reduction behavior of metal ions based on the analysis of changes in the UV-Vis spectra during ultrasonic irradiation.

4   Key Research Findings

4.1   Pd Nanoparticles

Pd nanoparticles can be widely applied to catalysts for cross-coupling reactions, hydrogenations and oxidations [27–29]. As described in the Introduction section, various preparation methods have been studied to prepare Pd nanoparticles. The size and shape of the nanoparticles are important factors to control their catalytic properties, because the surface structure and electronic state change depending on the size and shape of the nanoparticles. For example, the amount ratio of Pd atoms on the facets, edges, and corners of the nanoparticles changes when the size and shape of the nanoparticles change, resulting in the different catalytic activity for the structure sensitive reactions. By using a sonochemical reduction method, we can prepare size-controlled Pd nanoparticles [30]. We can see the characteristics of
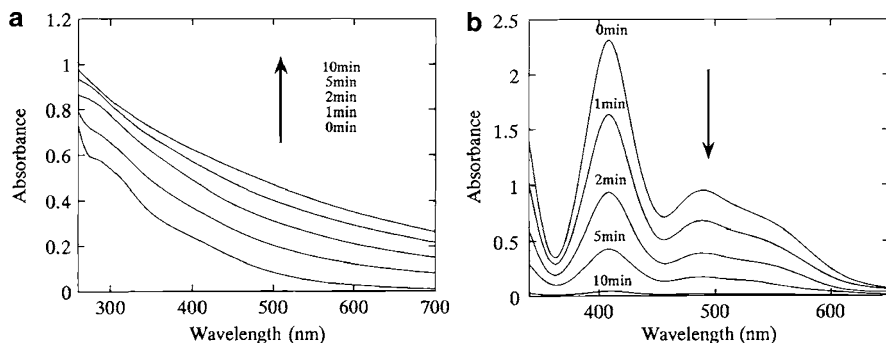
Fig. 4.3 (**a**) Changes in absorption spectra during ultrasonic irradiation of a Pd(II)-SDS aqueous solution under an argon atmosphere and (**b**) absorption spectra after addition of NaI to each sample solution of (**a**). Conditions: PdCl$_2$·2NaCl 0.5 mM, SDS 8 mM, cell length 0.5 cm (Reprinted with permission from Ref. [30]. Copyright 1996 American Chemical Society)

changes in the UV-Vis absorption spectra of a sample solution during ultrasonic irradiation.

Figure 4.3a shows changes in the absorption spectra during ultrasonic irradiation of an aqueous solution containing PdCl$_2$·2NaCl (hereafter, abbreviated to Pd(II)) and sodium dodecyl sulfate (SDS) under an argon atmosphere. Small absorption peaks at around 300 and 400 nm, characteristic of Pd(II), are observed before ultrasonic irradiation (corresponding to 0 min in Fig. 4.3a).

These peaks gradually disappear with irradiation and a broad absorption band between the UV and visible region appears. Based on the Mie theory [31], this broad band can be attributed to the spectrum of the solution containing colloidal Pd nanoparticles. The color of the solution changes from initial pale yellow to dark brown by ultrasonic irradiation. As a matter of fact, the formation of Pd nanoparticles must be confirmed by several analysis methods as described later.

To understand the mechanism of Pd(II) reduction and Pd nanoparticle formation, the concentration of Pd(II) should be measured as a function of irradiation time. However, it is impossible to determine the concentration of Pd(II) from the spectrum analysis of Fig. 4.3a. This is because the spectrum of Pd(II) in an aqueous solution consists of $[PdCl_x(H_2O)_{4-x}]^{(x-2)-}$ or $[PdCl_x(OH)_{4-x}]^{2-}$, which are dependent on the concentration of Pd(II) and the pH value of the solution. By using a NaI colorimetric method [30], the concentration of Pd(II) in the sample solution can be determined: the addition of an appropriate amount of a saturated NaI aqueous solution to the sample solution results in the formation of a Pd(II)-iodide complex with a large absorbance ($\varepsilon = 9,600$ M^{-1} cm^{-1} at wavelength of 408 nm) as seen in Eq. 4.8.

$$Pd(II) + 4I^- \rightarrow [PdI_4]^{2-} \tag{4.8}$$
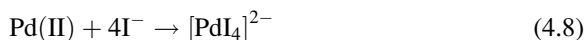
In addition, since the aggregation of colloidal Pd nanoparticles occurs simultaneously, the aggregated Pd nanoparticles can be removed by filtration with

a membrane filter. Therefore, based on this method, the concentration of Pd(II) in the sample solution can be spectrophotometrically determined without interference from surfactants and colloidal Pd nanoparticles. Figure 4.3b shows the absorption spectra obtained from each of the irradiated Pd(II) solutions in the presence of SDS after NaI addition and filtration with a 0.2-μm pore size membrane filter. The absorption peak attributed to $[PdI_4]^{2-}$ is clearly observed at 408 nm before ultrasonic irradiation, and the peak gradually decreases with increasing irradiation time.

In the presence of polyethylene(40)glycol monostearate (PEG40MS) instead of SDS, changes in the absorption spectra during irradiation were similar to those in the presence of SDS. On the other hand, in the case of a Pd(II)-polyvinyl pyrrolidone (PVP; Mw, 40,000) aqueous solution and a Pd(II)-polyoxyethylene (20)sorbitan monolaurate (Tween20) aqueous solution, different absorption spectra were observed: when NaI was added to the sample solution of Pd(II)-PVP or Pd(II)-Tween20, the absorption intensity and peak considerably changed ($\varepsilon = 21,000$ M^{-1} cm^{-1} at wavelength of 342 nm). These changes in the absorption spectra would be due to the fact that the coordination of PVP and Tween20 to Pd(II) partly occurred. However, a good linear line dependence of absorbance versus concentration of Pd(II) was able to be obtained as in the SDS and PEG40MS solutions.

By using the colorimetric method, the rates of reduction of Pd(II) can be measured and analyzed. For example, when the types of added organic additives were changed, it was found from the analysis of the colorimetric method that the rates changed in the order of no organic additive (6.9 μM min^{-1}) < 1 g/L PVP (87 μM min^{-1}) < 8 mM SDS (130 μM min^{-1}) < 0.4 mM PEG40MS (230 μM min^{-1}) < 5 g/L Tween20 (400 μM min^{-1}), at an initial concentration of 1.0 mM of Pd(II) [30]. In addition, when the concentration of SDS was increased, the rates of reduction of Pd(II) also increased as 30 μM min^{-1} at 0.1 mM SDS < 100 μM min^{-1}, at 1 mM SDS < 130 μM min^{-1}, and at 8 mM SDS. Even in the case of the addition of alcohols or carboxylic acids, the rates can be changed. For example, the rates were 250 μM min^{-1} in a 10 mM t-BuOH aqueous solution and 300 μM min^{-1} in a 10 mM n-pentanoic acid aqueous solution. Based on these results, it was concluded that organic additives act as a precursor for the formation of reductants as described in the mechanism of the sonochemical reduction. Therefore, the concentration and types of organic additives are important factors to control the rates of reduction.

Figure 4.4 shows a TEM image of Pd nanoparticles formed from the sonolysis of a 1.0 mM Pd(II) and 0.4 mM PEG40MS aqueous solution. It can be seen that the size of the Pd nanoparticles is ca. 5 nm [10]. Since organic additives of PVP, SDS, PEG40MS, and Tween20 act as colloidal stabilizers to suppress the aggregation of Pd nanoparticles, the synthesis of the size-controlled Pd nanoparticles can be performed by using these stabilizers. The average size of the sonochemically formed Pd nanoparticles decreased with decreasing initial concentrations of Pd(II) [30]. In addition, the average size decreased with increasing rates of Pd(II) reduction [32].

Fig. 4.4 TEM image of sonochemically prepared Pd nanoparticles from the reduction of 1.0 mM Pd(II) and 0.4 mM PEG40MS (Reprinted with permission from Ref. [10]. Copyright 1996 Elsevier)
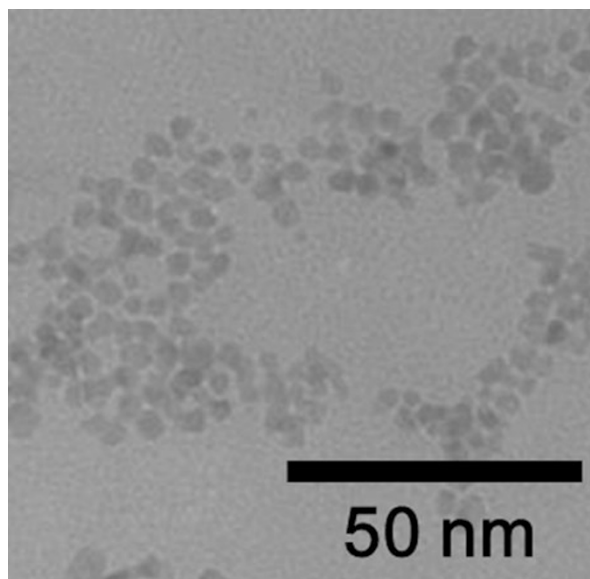
The types of precursors also affect the reduction behavior of metal ions and formation behavior of metal nanoparticles. When a $[Pd(NH_3)_4]Cl_2$ aqueous solution is sonicated instead of $PdCl_2 \cdot 2NaCl$, the rate of reduction is different. Figure 4.5a shows changes in the absorption spectra of a $[Pd(NH_3)_4]Cl_2$ aqueous solution containing 2-propanol during ultrasonic irradiation [33]. A broad absorption band between the UV and visible region increases with increasing irradiation time, and an absorption peak can be observed at 225 nm at the irradiation times of 30, 60, and 120 min. Creighton and Eadon [31] reported that the calculated surface plasmon peak of spherical Pd nanoparticles of 10 nm diameter in water was located at 220–230 nm. In most cases, it is difficult to confirm the peak at 220–230 nm experimentally because it is often overlapped with other absorption spectra of coexisting solutes such as inorganic ions and organic stabilizers.

However, if the spectrum interference due to coexisting solutes was removed, the absorption spectra should become clearer. Figure 4.5b and c shows absorption spectra of sonochemically formed Pd nanoparticles before and after corrections in the region from 200 to 280 nm, where the corrected absorption spectra (Fig. 4.5c) are prepared by abstracting the spectra of $[Pd(NH_3)_4]Cl_2$ remaining in the irradiated solution from the spectra of Fig. 4.5b. In this case, the concentrations of $[Pd(NH_3)_4]$ Cl_2 are measured first by the colorimetric method, and then, the overlapping spectra are removed from the uncorrected absorption spectra. Since the mole absorption coefficient of Cl^- and NH_4^+ ions is quite small compared with that of $[Pd(NH_3)_4]$ Cl_2, the corrections for these ions are excluded. As seen in Fig. 4.5c, the clear peak corresponding to the surface plasmon of the Pd nanoparticles can be seen after the spectrum corrections.
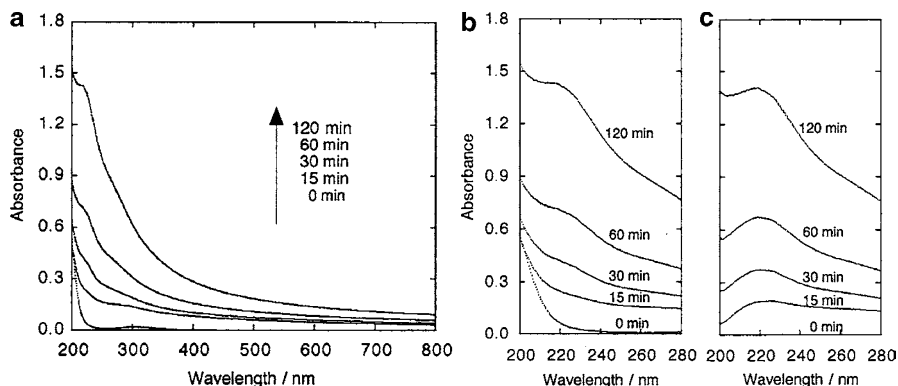
Fig. 4.5 (**a**) Changes in the absorption spectra of $[Pd(NH_3)_4]Cl_2$ solution in the presence of 2-propanol during ultrasonic irradiation. (**b**) Absorption spectra of sonochemically formed Pd nanoparticles before and (**c**) after corrections. Conditions: 0.2 mM $[Pd(NH_3)_4]Cl_2$, 100 mM 2-propanol, argon atmosphere, cell length, 0.5 cm (Reprinted with permission from Ref. [33]. Copyright 2002 The Chemical Society of Japan)

The TEM analysis indicated that the size of the formed Pd nanoparticles was about 20–30 nm. The Pd nanoparticles formed here were stable in the colloidal state for more than 6 months, although no stabilizer existed in the solution.

Based on the colorimetric method, we can measure the rates of $[Pd(NH_3)_4]^{2+}$ reduction during ultrasonic irradiation. Although the sonochemical reduction of $[Pd(NH_3)_4]^{2+}$ did not proceed in the absence of 2-propanol, it proceeded in the presence of 2-propanol, where the rate was estimated to be 2.1 $\mu M\,min^{-1}$ at 0.2 mM $[Pd(NH_3)_4]^{2+}$. Consequently, it was found that the rate of $[Pd(NH_3)_4]^{2+}$ reduction was slower than that of the Pd(II) (= $PdCl_2 \cdot 2NaCl$) reduction, indicating that $[Pd(NH_3)_4]^{2+}$ is more stable than Pd(II) for the reducing species formed from the sonolysis of water and 2-propanol.
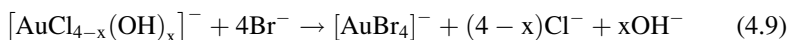
4.2   Au Nanoparticles

Au nanoparticles can be widely applied to various fields of nanotechnology such as catalysts [34–36], sensors [37, 38], and surface-enhanced Raman spectroscopy [39]. By using a sonochemical reduction method, we can prepare Au nanoparticles. Figure 4.6a shows a representative spectrum change in the solution containing $NaAuCl_4$ (hereafter, abbreviated to Au(III)) and SDS during ultrasonic irradiation [40]. The absorption peak at around 300 nm can be observed before ultrasonic irradiation. This peak corresponds to $[AuCl_{4-x}(OH)_x]^-$ [41]. After irradiation, a new absorption peak appears at around 530 nm, and its intensity gradually increases with increasing irradiation time, indicating the formation of Au nanoparticles. It is also clear that the
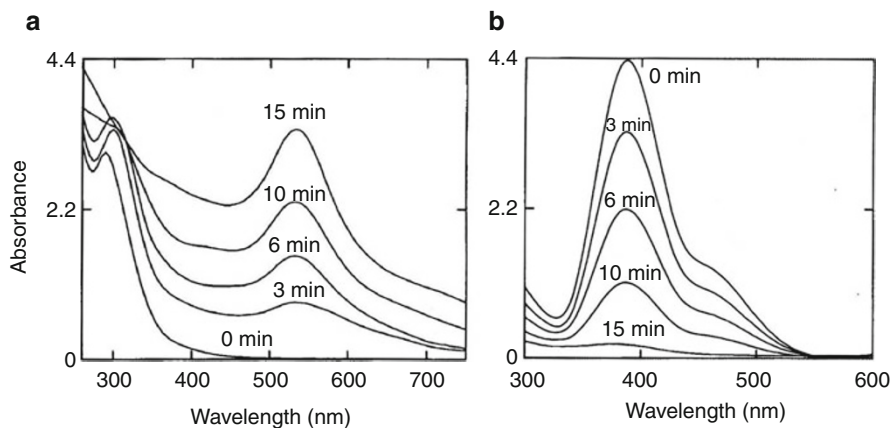
Fig. 4.6 (**a**) Changes in absorption spectra during ultrasonic irradiation of Au(III)-SDS aqueous solution under an argon atmosphere and (**b**) absorption spectra after addition of NaBr to the sample solution of (**a**). Conditions: NaAuCl$_4$ 1 mM, SDS 8 mM, cell length 1.0 cm (Reprinted with permission from Ref. [40]. Copyright 1996 Radiation Research Society)

absorption peak corresponding to $[AuCl_{4-x}(OH)_x]^-$ disappears at 15 min irradiation. In this case, the color of the sample solution gradually changes from initial yellow to reddish-violet by ultrasonic irradiation.

It is clear that the concentration of $[AuCl_{4-x}(OH)_x]^-$ cannot be measured correctly from the analysis of Fig. 4.6a because the spectrum of Au nanoparticles overlaps with that of $[AuCl_{4-x}(OH)_x]^-$ during ultrasonic irradiation, and thus, the peak corresponding to $[AuCl_{4-x}(OH)_x]^-$ shifts. However, when the addition of a NaBr solution to the sample solution of Fig. 4.6a is performed, the concentration of $[AuBr_4]^-$ formed from $[AuCl_{4-x}OH_x]^-$ can be measured as seen in Fig. 4.6b, where the following ligand exchange reaction occurs:

$$\left[AuCl_{4-x}(OH)_x\right]^- + 4Br^- \rightarrow [AuBr_4]^- + (4-x)Cl^- + xOH^- \qquad (4.9)$$

Simultaneously, the aggregation of colloidal Au nanoparticles occurs. Since the aggregated Au nanoparticles can be removed by filtration, the concentration of unreduced Au(III) can be determined, and the rate of reduction of Au(III) can be calculated to be 83 μM min^{-1}. The rates of reduction of Au(III) are strongly dependent on the types and concentrations of organic additives [40] and the types of dissolved gases [11].

The average size of the formed Au nanoparticles has been measured to be 10 and 9 nm from the analysis of dynamic light scattering and TEM, respectively [40]. Recently, Haiss et al. reported a simple method to estimate the size of Au nanoparticles from the analysis of an UV-Vis spectrum [42]. They plotted the ratio of the surface plasmon resonance peak (A_{spr}) to the absorbance at 450 nm (A_{450}) as a function of the logarithm of the particle diameter (D), where the plots

were prepared by use of the theoretical and experimental data, respectively. As a result, the linear relationship between A_{spr}/A_{450} and D was established in the size range from 5 to 80 nm as follows:

$$D = \exp(B_1 \frac{A_{spr}}{A_{450}} - B_2) \qquad (4.10)$$

where B_1 is the inverse of the slope (m) of the linear fit, B_2 is B_0/m, and B_0 is the intercept. They found from the theoretical data that B_1 and B_2 were 3.55 and 3.11, respectively. On the other hand, from the experimental data, B_1 and B_2 were 3.00 and 2.20, respectively.

By using the theoretically and experimentally measured values of B_1 and B_2, the diameter of the sonochemically formed Au nanoparticles at 15 min irradiation in Fig. 4.6a can be calculated to be 8.8 and 9.7 nm, respectively. These values are in good agreement with those measured by dynamic light scattering and TEM. The size of the sonochemically formed Au nanoparticles can be controlled by various parameters such as types of organic additives and dissolved gas, intensity of ultrasound, frequency of ultrasound, and distance between the reaction vessel and the oscillator [11, 26].

4.3   Pt Nanoparticles

Pt nanoparticles can be applied to various catalysts for electrocatalytic oxidations [43, 44] and water-gas shift reactions [45]. A sonochemical reduction method can be used to prepare Pt nanoparticles [10, 46, 47]. Figure 4.7a shows changes in the absorption spectra during ultrasonic irradiation to an aqueous solution containing K_2PtCl_4 (hereafter, abbreviated to Pt(II)) and SDS [46]. Small absorption peaks at 380.5 and 317.5 nm attributed to Pt(II) gradually disappear, and a broad absorption band between the UV and visible region increases with increasing irradiation time. This spectrum change is due to the progress of the reduction of Pt(II) and formation of Pt nanoparticles.

The absorption spectrum of Pt(II) is unclear as seen in Fig. 4.7a, because Pt(II) in water consists of $[PtCl_x(H_2O)_{4-x}]^{(x-2)-}$ or $[PtCl_x(OH)_{4-x}]^{2-}$. However, the concentration of Pt(II) can be determined by the NaI colorimetric method as follows:

$$Pt(II) + 4I^- \rightarrow PtI_4^{2-} \qquad (4.11)$$

Since the aggregated Pt nanoparticles that are induced by the addition of NaI can be removed by filtration, the absorption spectra of PtI_4^{2-} attributed to Pt(II) can be clearly measured as seen in Fig. 4.7b. The spectrum and TEM analyses indicated that the rate of Pt(II) reduction and the average size of the formed Pt nanoparticles were measured to be 26.7 μM min^{-1} and 2.6 nm, respectively [46].

In the following section, we look at the sonochemical reduction of the different valence of the Pt precursor. Figure 4.8a shows changes in the absorption spectra
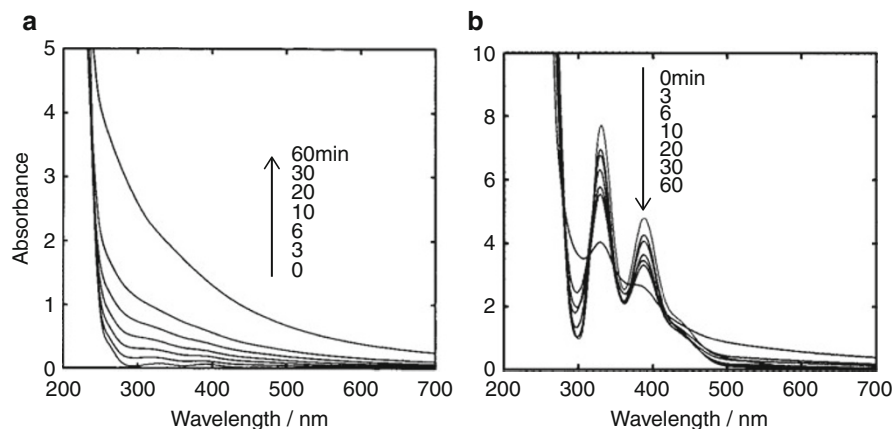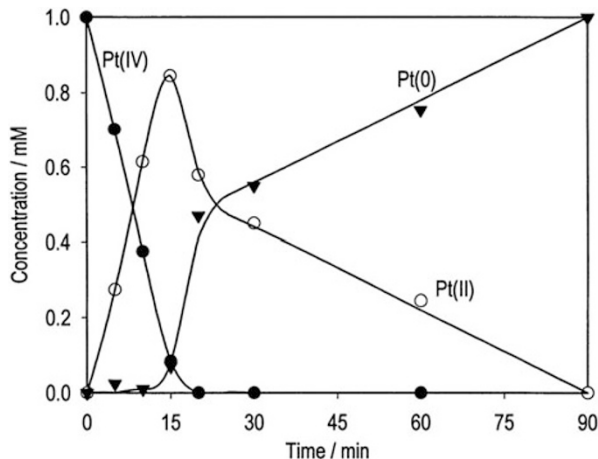
Fig. 4.7 (**a**) Changes in the absorption spectra of a solution of K_2PtCl_4 and SDS during ultrasonic irradiation under an argon atmosphere and (**b**) absorption spectra of NaI treated sample solution of (**a**). Conditions: K_2PtCl_4 1 mM, SDS 8 mM (Reprinted with permission from Ref. [46]. Copyright 1999 American Chemical Society)
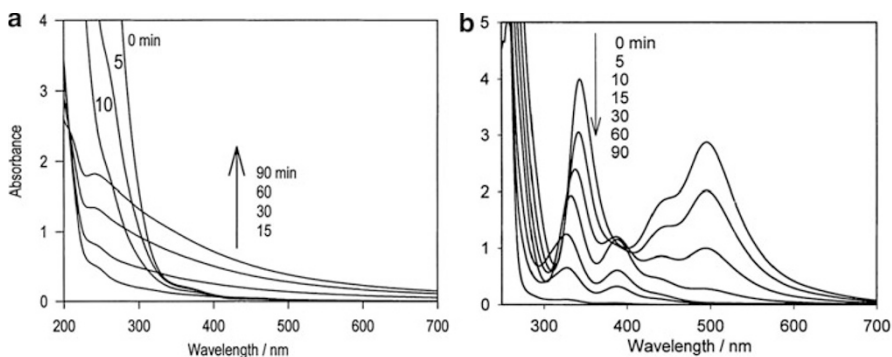
Fig. 4.8 (**a**) Changes in the absorption spectra of a solution of H_2PtCl_6 and SDS during ultrasonic irradiation under an argon atmosphere and (**b**) absorption spectra of NaI treated sample solution of (**a**). Conditions: H_2PtCl_6 1 mM, SDS 8 mM (Reprinted with permission from Ref. [47]. Copyright 2001 Elsevier)

during ultrasonic irradiation of an aqueous solution containing H_2PtCl_6 (hereafter, abbreviated to Pt(IV)) and SDS [47]. It can be seen that the absorbance in the UV region attributed to Pt(IV) decreases with increasing irradiation time from 0 min to 15 min. After 15 min irradiation, a broad absorption band between the UV and visible region increases with increasing irradiation time. This spectrum change is due to the consecutive progress of the reduction of Pt(IV) to Pt(II) and Pt(II) to Pt(0) (corresponding to the formation of Pt nanoparticles) as described later.

Fig. 4.9 Changes in the concentrations of Pt(IV), Pt(II), and Pt(0) during ultrasonic irradiation of an argon saturated aqueous solution containing 1 mM H_2PtCl_6 and 8 mM SDS (Reprinted with permission from Ref. [47]. Copyright 2001 Elsevier)

Similar to Pt(II), the following ligand exchange reaction of Pt(IV) (Pt(IV) in water consisting of $[PtCl_{6-x}(H_2O)_x]^{(2-x)-}$ or $[PtCl_{6-x}(OH)_x]^{2-}$) occurs after addition of a saturated NaI solution to the sample solution of Fig. 4.8a.

$$Pt(IV) + 6I^- \rightarrow PtI_6{}^{2-} \tag{4.12}$$

Therefore, the absorption spectra of $PtI_6{}^{2-}$ attributed to Pt(IV) can be measured as seen in Fig. 4.8b, where the formation of $PtI_4{}^{2-}$ (Pt(II)) is also confirmed as an intermediate during the sonochemical reduction of Pt(IV).

From the analysis of Fig. 4.8b, changes in the concentrations of Pt(IV), Pt(II), and Pt(0) during ultrasonic irradiation can be prepared as shown in Fig. 4.9. It is clear that the reduction of Pt(IV) proceeds to form Pt(II) and then the reduction of Pt(II) to Pt(0) proceeds consecutively [47].

It has also been reported that the reduction rates of Pt(IV) to Pt(II) were strongly affected by the concentration and types of organic stabilizers of SDS, PEG40MS, and sodium dodecylbenzenesulfonate, although those of Pt(II) to Pt(0) were hardly affected. The average sizes of the formed Pt nanoparticles at 8 mM SDS and 0.4 mM PEG40MS were measured to be ca. 3 nm and ca. 1 nm, respectively [47].

4.4 Ag Nanoparticles

Ag nanoparticles have been investigated actively from the fundamental point of view to understand the mechanism of Ag(I) reduction and Ag nanoparticle formation. This would be because Ag(I) is a simple monovalent metal cation, and the formed Ag clusters have a size-dependent absorption property. In addition, Ag nanoparticles can be widely applied to various technologies such as surface-enhanced Raman spectroscopy [48] and optical sensing [49, 50].

Fig. 4.10 Changes in absorption spectra of AgNO$_3$−PVP solution during ultrasonic irradiation under an argon atmosphere. Conditions: 0.5 mM of AgNO$_3$, 1 g/L of PVP [52]
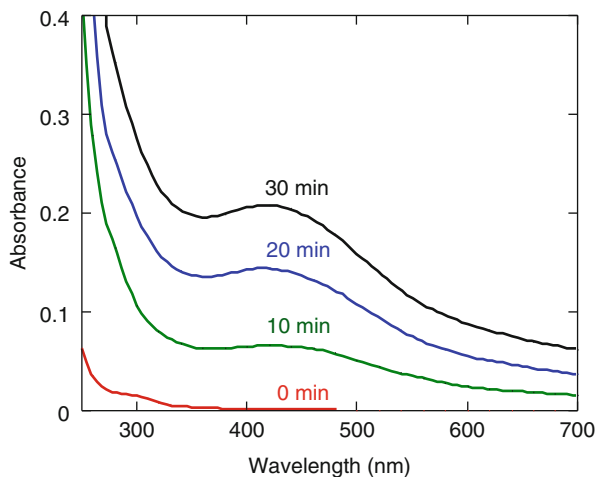
Nagata et al. reported the formation of Ag nanoparticles from the sonochemical reduction of Ag(I), where AgClO$_4$ or AgNO$_3$ were used as precursors [51]. An example for changes in the absorption spectra of an aqueous solution containing AgNO$_3$ and PVP during irradiation is shown in Fig. 4.10 [52]. Although little absorption is observed before irradiation, a new absorption peak at around 420 nm gradually emerges with irradiation time. It is clear that the concentration of Ag(I) cannot be measured by analyzing the spectra of Fig. 4.10. To measure the amount of the formed Ag(0) colorimetrically, Nagata et al. used Eq. 4.13:

$$Ag(0) + C(NO_2)_4 \rightarrow Ag(I) + C(NO_2)^{3-} + NO_2 \tag{4.13}$$
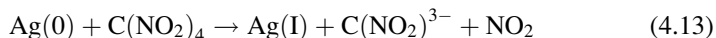
where the absorbance of C(NO$_2$)$^{3-}$ (ε =14,000 M^{-1} cm^{-1} at wavelength of 350 nm) was measured. By analyzing the amount of C(NO$_2$)$^{3-}$, the reduction rate of Ag(I) can be estimated. Ag nanoparticles can be also synthesized in the presence of other stabilizers such as SDS, PEG40MS and Tween20. The average size of the Ag nanoparticles formed from the sonochemical reduction of AgClO$_4$-PEG40MS was measured to be 13 nm, as determined by a dynamic light scattering photometer.

Gedanken et al. reported the formation of Ag nanoparticles from the sonochemical reduction of Ag(I) in the absence of organic additives under an argon-hydrogen atmosphere [53]. Zhu et al. reported the formation of Ag nanorods from the sonochemical reduction of Ag(I) in the presence of methenamine and PVP [54].

Xu and Suslick recently reported that very small Ag nanoparticles with a highly fluorescent property (hereafter, abbreviated to Ag nanoclusters) can be prepared by the sonochemical reduction of Ag(I) in the presence of polymethylacrylic acid (PMAA), which acts as a capping agent [55]. We can observe changes in the absorption spectra during the formation of Ag nanoclusters. They used a horn-type sonicator (1 cm^2 Ti horn at 20 kHz and 25 W cm^{-2}) to prepare Ag nanoclusters under an argon atmosphere at 20 °C. Figure 4.11a shows changes in the absorption
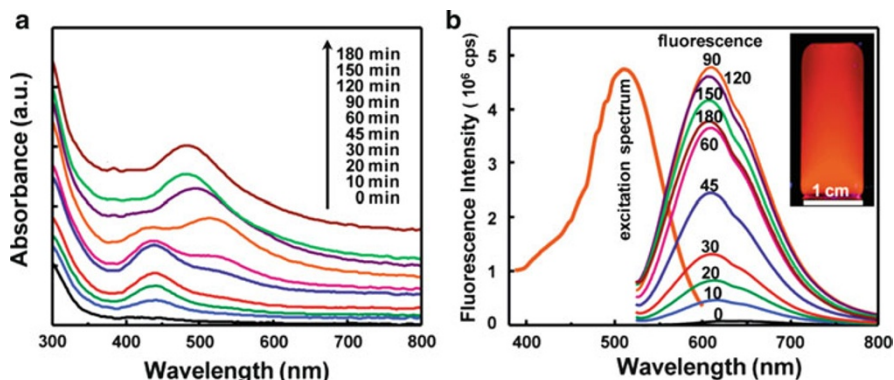
Fig. 4.11 (**a**) UV-Vis spectra and (**b**) fluorescence emission spectra of the solution containing PMAA and AgNO$_3$ after increasing length of sonication time; the excitation spectrum shown in (**b**) corresponds to the 90-min sample with an emission wavelength of 610 nm (*inset*: solution of the Ag nanoclusters illuminated by a UV lamp with 365-nm excitation) (Reprinted with permission from Ref. [55]. Copyright 2010 American Chemical Society)

spectra of an aqueous solution containing Ag(I) and PMAA during ultrasonic irradiation. The formation of Ag nanoclusters can be confirmed by an absorption peak at around 440–520 nm, which gradually emerges by ultrasonic irradiation. In this case, the color of the solution gradually changes from colorless (0 min) to pink (90 min) and then dark red (180 min). The formed Ag nanoclusters were measured to be less than 2 nm in diameter.

Since the carboxylic acid groups in PMAA have a strong affinity for Ag(I) ions and Ag metal surfaces, the aggregation of Ag nanoclusters would be suppressed. The formed Ag nanoclusters have a high fluorescent property, as seen in the inset of Fig. 4.11b. They also reported that the optical and fluorescence properties of the sonochemically synthesized Ag nanoclusters also change by modifying the stoichiometry of the carboxylate groups of PMAA to Ag(I) [55]. In general, Ag nanoclusters can be applied to fluorescent sensors for metal ions such as Cu(II) [49] and Hg(II) [50]. More recently, it has been reported that Au/Ag nanoclusters with a yellow emission can be synthesized by ultrasonic irradiation in the presence of bovine serum albumin [56].

4.5   Reduction Mechanism of Metal Ions

The reduction of Pd(II), Au(III), Pt(II), Pt(IV), and Ag(I) proceeds by ultrasonic irradiation as described before. Here, the reduction behavior among Pd(II), Au(III), Pt(II), and Ag(I) in the presence of SDS will be compared by analyzing the rates of reduction. Based on Eqs. 4.1–4.6, various types of reductants are formed in the sonolysis of SDS and water. Since each of the reductants should have different reducing potentials for metal ions, the rate of reduction of metal ions should depend on the reactivity of the metal ions with reductants.

In the case of 200 kHz ultrasonic irradiation under an argon atmosphere, the rates of the sonochemical reduction are reported to be in the order of 130 $\mu M\ min^{-1}$ for Pd(II) > 83 $\mu M\ min^{-1}$ for Au(III) > 19 $\mu M\ min^{-1}$ for Pt(II) > 7 $\mu M\ min^{-1}$ for Ag(I) [10]. Since metal ions have different valences, the rates of the sonochemical reduction should be corrected for comparison with each other. If the rates were corrected on the basis of the number of electron transfers (e.g., Pd(II) needs two electrons to form Pd(0) and Au(III) needs three electrons to form Au(0)), the order would become Pd(II) $\approx$ Au(III) > Pt(II) > Ag(I). This order does not agree with the order of the redox potential of each metal ion. It is found that the rates of the sonochemical reduction of Pt(II) and Ag(I) are considerably slower than those of Pd(II) and Au(III). From the analysis of the reduction behavior during gamma ray irradiation under a N_2O atmosphere [10], it is suggested that the sonochemical reduction of Pt(II) and Ag(I) proceeds mainly via the reduction by •R and H_2, which are formed by the abstraction reactions as Eq. 4.2. On the other hand, in the cases of Pd(II) and Au(III), the sonochemical reduction proceeds mainly via the reduction by pyrolysis radicals and unstable products, which are formed by the pyrolysis of RH as Eq. 4.3.

To evaluate the effects of •R and H_2 on the reduction of metal ions, the analysis of the amount of H_2O_2 formed in the sonolysis of pure water is useful, because the amount of H_2O_2 should be related to that of •R and H_2, taking into account Eqs. 4.2 and 4.7. As a result of this analysis, the effects of the pyrolysis radicals and unstable products on the reduction of the metal ions can also be evaluated as seen in the literature [10, 11, 26, 30, 32, 33, 40, 46, 47].
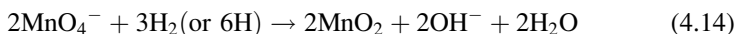
4.6   MnO$_2$ Nanoparticles

MnO_2 is a useful material for application to electrochemical capacitors, Li-batteries, sensors, and catalysts [57–60]. Okitsu et al. reported that the sonochemical reduction of MnO_4^- occurs to form MnO_2 nanoparticles [9]. Figure 4.12a and b shows changes in the absorption spectra of a MnO_4^- aqueous solution during ultrasonic irradiation, where no organic compound has been added. During irradiation, the color of the sample solution gradually changes from purple (0 min) to pale yellow (8 min) and finally turned to colorless (12, 14, 16 min). Figure 4.12a shows that several absorption peaks of MnO_4^- from 450 to 580 nm gradually disappear, and a new broad peak at around 360 nm emerges by ultrasonic irradiation. Based on the literature [61–64], this new peak can be attributed to colloidal MnO_2 particles. Therefore, a pale yellow color solution at 8 min irradiation corresponds to the formation of colloidal MnO_2 particles. In Fig. 4.12a, two isosbestic points are also observed at 504 and 580 nm, indicating that the reduction of MnO_4^- to MnO_2 proceeds consecutively by ultrasonic irradiation. Figure 4.12b shows changes in the absorption spectra following further irradiation. The peak at around 360 nm quickly decreases with increasing irradiation time. This is due to the progress of the reduction of MnO_2 to Mn^{2+} [62, 64].
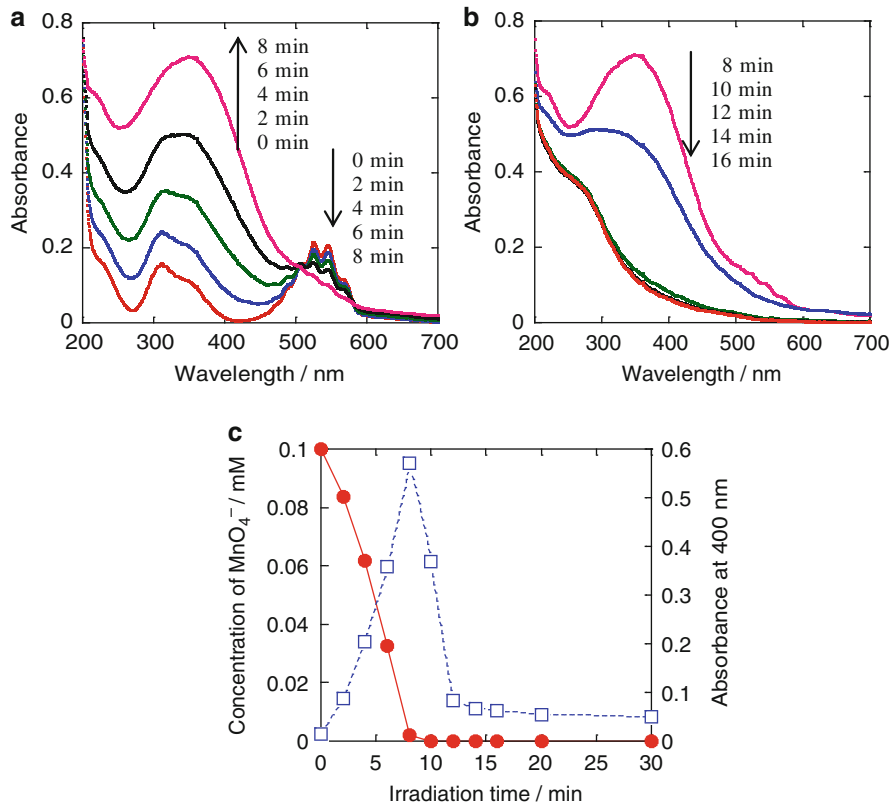
Fig. 4.12 (**a**) Changes in absorption spectra of MnO_4^- aqueous solution before and after 2, 4, 6, and 8 min ultrasonic irradiation and (**b**) after 8, 10, 12, 14, and 16 min ultrasonic irradiation. (**c**) Changes in the concentration of MnO_4^- (●) and absorbance at 400 nm (□) during ultrasonic irradiation. Initial concentration of MnO_4^-: 0.1 mM, argon atmosphere (Reprinted with permission from Ref. [9]. Copyright 2009 Elsevier)

Figure 4.12c shows changes in the concentration of MnO_4^- during ultrasonic irradiation. As an index of the amount of MnO_2 in the sample solution, changes in the absorbance at 400 nm are also plotted, where the absorbance at 400 nm is chosen to reduce the overlap of the MnO_4^- absorbance. It is clear that the formation of MnO_2 occurs along with the reduction of MnO_4^-, and the formed MnO_2 is reduced consecutively by further irradiation. From Fig. 4.12c, it is found that 8 min irradiation is the optimum irradiation time to prepare MnO_2 particles.

In this study, since no organic additive is added to the sample solution, the reduction of MnO_4^- proceeds as follows:

$$2MnO_4^- + 3H_2(or\ 6H) \rightarrow 2MnO_2 + 2OH^- + 2H_2O \qquad (4.14)$$

$$2MnO_4^- + 3H_2O_2 \rightarrow 2MnO_2 + 3O_2 + 2OH^- + 2H_2O \qquad (4.15)$$

where MnO_4^- can react with H_2O_2 because of the strong oxidizing agent of MnO_4^- [65]. As seen in Eqs. 4.14 and 4.15, the measurement of pH is also useful to understand the progress of the formation of MnO_2.

4.7   Au Core/Pd Shell Nanoparticles

Bimetallic nanoparticles of Au/Pd can be prepared by sonochemical reduction of the corresponding metal ions [66–69]. Au/Pd nanoparticles are recently researched as active catalysts that can be applied to various catalytic reactions such as alkene hydrogenation [67, 68], H_2O_2 production [70], and CO oxidation [71]. Figure 4.13a shows changes in the absorption spectra of the sample solution containing Au(III), Pd(II), and SDS during ultrasonic irradiation [66]. It can be seen that an absorption peak at around 520 nm gradually emerges with increasing irradiation time and becomes clear at 6 min irradiation. This peak is in good agreement with the surface plasmon peak of Au nanoparticles [31, 40]. After that, the peak becomes broader following further irradiation. The color of the solution gradually changes from pale yellow (0 min) to reddish-violet (6 min) and finally to dark brown (15 min) during ultrasonic irradiation.

Figure 4.13b shows changes in the concentrations of Au(III) and Pd(II) during ultrasonic irradiation, where the concentrations are measured using a colorimetric method [66]. It can be seen that the reduction of Au(III) starts at first and then the reduction of Pd(II) starts after completion of the reduction of Au(III). The TEM analysis indicated that the average size of the formed Au/Pd nanoparticles is ca. 8 nm and they have a Au core and a Pd shell nanostructure. Based on the formation of the core/shell nanostructure, it can be concluded that the reason why the surface plasmon peak of Au nanoparticles becomes broader at 9 min irradiation is because of the deposition of the sonochemically reduced Pd atoms on the formed Au nanoparticles. As seen in Fig. 4.13a and b, the analysis of the UV-Vis spectra is an important probe to understand the reduction behavior of Pd(II) and Au(III) as well as the formation behavior of Au core/Pd shell nanoparticles.

4.8   Au Nanorods

Rod-shaped Au nanoparticles (Au nanorods) have great potential in a wide variety of applications such as photothermal therapy of cancer cells [72] and optical data storage [73]. Okitsu et al. reported the synthesis of Au nanorods from the sonochemical reduction of Au(I) [74]. Figure 4.14 shows changes in the extinction spectra of the sample solution during ultrasonic irradiation at pH 3.5. Cetyltri-methylammonium bromide (CTAB), $AgNO_3$, and ascorbic acid are added to the solution of $HAuCl_4$, where CTAB and $AgNO_3$ act as shape-control agents and ascorbic acid acts as a weak reductant to reduce $HAuCl_4$ to Au(I). From this figure, the term of extinction is used instead of absorbance, because Au nanorods have a light scattering property depending on their size and shape. Therefore, the term of
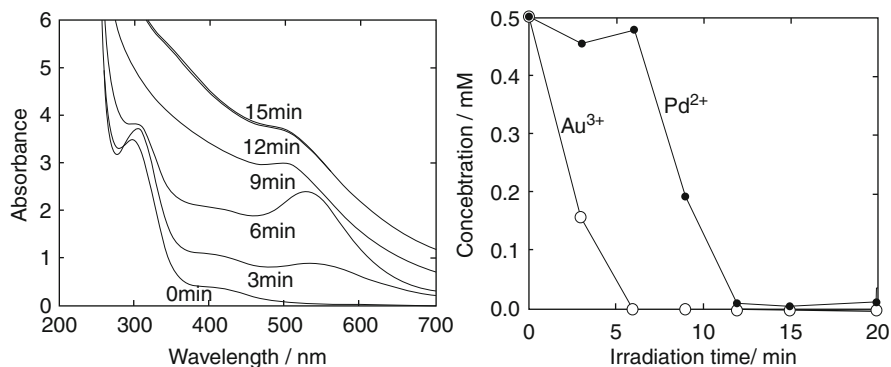
Fig. 4.13 (**a**) Changes in the absorption spectra of sample solution containing Au(III), Pd(II), and SDS during ultrasonic irradiation. (**b**) Changes in the concentrations of Au(III) and Pd(II) during ultrasonic irradiation of an aqueous solution. Conditions: 0.5 mM NaAuCl$_4$, 0.5 mM PdCl$_2$·2NaCl and 8 mM SDS, argon atmosphere (Reprinted with permission from Ref. [66]. Copyright 1997 American Chemical Society)
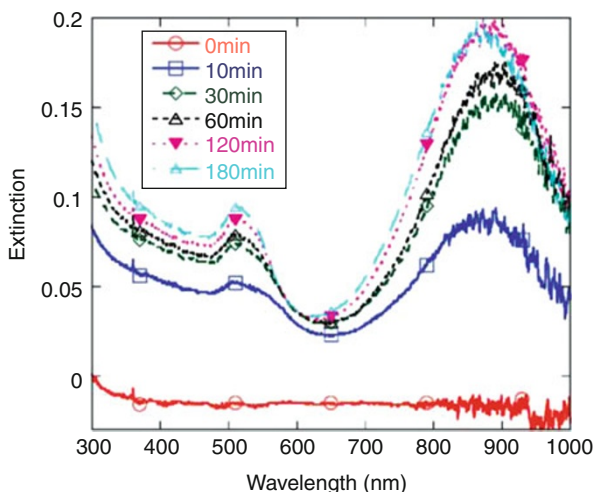
Fig. 4.14 Changes in extinction spectra of sample solution of Au(I) during ultrasonic irradiation under an argon atmosphere at pH 3.5. Cell length: 0.5 cm (Reprinted with permission from Ref. [74]. Copyright 2009 American Chemical Society)

extinction is appropriate for the results of UV-Vis spectroscopy. In Fig. 4.14, it can be seen that the extinction intensity gradually increases with irradiation time, and extinction peaks at around 510 and 880 nm are clearly observed at the irradiation time from 10 to 180 min. These peaks correspond with the surface plasmon bands of Au nanorods [3, 75, 76], indicating that the reduction of Au(I) to Au(0) proceeds and formation of Au nanorods occurs.

Figure 4.15a shows a TEM image of Au nanoparticles formed at 180 min irradiation in Fig. 4.14. It is clear that rod-shaped nanoparticles are formed in the size range of 10–50 nm. Figure 4.15b shows the distribution of the aspect ratio measured. It is found that the formation of nanorods with an aspect ratio
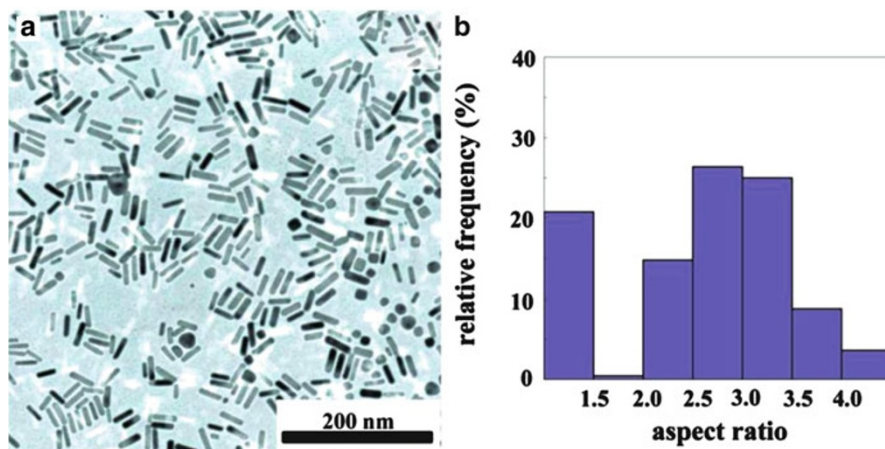
Fig. 4.15 (**a**) TEM image of Au nanorods and nanoparticles formed after irradiation of a sample solution of Au(I) under an argon atmosphere at pH 3.5 for 180 min. (**b**) Distribution of the aspect ratio of Au nanorods and nanoparticles (Reprinted with permission from Ref. [74]. Copyright 2009 American Chemical Society)

from 1.5 to 2.0 is almost zero. From Fig. 4.15a and b, spherical-, cubic-, and irregular-shaped particles with an aspect ratio of less than 1.5 are formed partly, and the total yield of these is measured to be ca. 20 %. The average aspect ratio of the formed nanorods was 3.0, when particles with an aspect ratio of less than 1.5 were excluded from the calculation of the average aspect ratio. Since Fig. 4.14 shows that the peak wavelength of the surface plasmon bands hardly changes during ultrasonic irradiation, it is possible that the formation of nanorods is determined at the initial growth stage of the formed Au seeds.

The pH of the solution is one of the important factors to control the sonochemical reduction of Au(I) and formation of Au nanoparticles. Figure 4.16 shows the extinction spectra of the sonochemically formed Au nanoparticles after 180 min irradiation of different pH solutions. It can be seen that the peak wavelength of the longitudinal plasmon band decreases as the pH of the solution increases.

The TEM analysis indicated that the average aspect ratio of Au nanorods synthesized at different pH solutions decreased as follows: 3.0 at pH 3.5 < 2.2 at pH 5.0 and < 2.1 at pH 6.5, where particles with an aspect ratio of less than 1.5 were excluded from the calculation of the average aspect ratio. This order can be connected to the order of the peak shift observed in the extinction spectra as seen in Fig. 4.16: the peak wavelength of the longitudinal plasmon band decreases with decreasing aspect ratio of the formed Au nanorods.

As seen in the results for Au nanorods, the extinction spectrum changes strongly depending on the aspect ratio of Au nanorods. In the case of the synthesis of shape-controlled nanoparticles with a surface plasmon peak, therefore, the analysis of the extinction spectrum is an important probe to know the average property of the

Fig. 4.16 Effects of pH on the extinction spectra of Au nanorods and nanoparticles formed after irradiation of sample solutions of Au(I) under an argon atmosphere for 180 min. Cell length: 0.5 cm (Reprinted with permission from Ref. [74]. Copyright 2009 American Chemical Society)
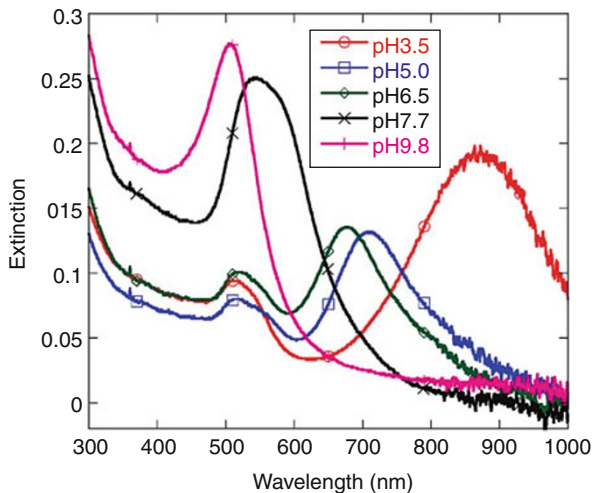
formed nanoparticles in the state of the colloidal dispersion system. In the analysis of a TEM image, a large number of particles must be analyzed to get the average information of the formed nanoparticles. In addition, it is possible that the preparation processes of the TEM specimens affect the formation of some aggregation with nanostructures. For example, the following phenomena may occur [74]: (1) during the processes of centrifugation to remove dissolved organic and inorganic species in solution, some aggregation of nanoparticles may occur, and (2) during the addition of a sample solution to a TEM grid or during the drying processes of a sample solution on a TEM grid, some aggregation of the nanoparticles may occur. In such a case, chemical reactions of the nanoparticles or unreduced metal ions with a TEM grid such as Cu may be induced to form some aggregation and/or unexpected nanostructures. Therefore, the results of TEM showing the formation of the unique shape should be compared with those of the extinction spectrum of the sample solution to confirm whether the formation of nanostructures occurs in the state of the colloidal dispersion system or not.

5   Conclusions and Future Perspective

UV-Vis spectroscopy provides important information about the sonochemical reduction processes of metal ions and the formation processes of metal nanoparticles in solution. In this chapter, the optical properties of spherical nanoparticles of Pd, Au, Pt, Ag, MnO_2, and core/shell bimetal nanoparticles and shape-controlled nanoparticles are described mainly on the basis of changes in the UV-Vis spectra during ultrasonic irradiation. It is noted that the UV-Vis spectrum has to be collected as a function of irradiation time to understand the effects of ultrasound on the synthesis of these nanoparticles. Since the reduction processes of metal ions can be linked to the formation processes of metal nanoparticles,

the analysis of both processes must be performed to understand the mechanism. In particular, since the analysis of the UV-Vis spectrum of the nanoparticle sample solution corresponds to real information for the formed metal nanoparticles in the state of a colloidal dispersion system, the analysis of the spectrum must be performed comprehensively. In the case of the synthesis of shape-controlled nanoparticles, it is probable that the analysis of TEM only leads to misunderstandings when the preparation and analysis of the TEM sample are not performed adequately. Therefore, to evaluate the formed nanoparticles correctly, the results of the TEM analysis should be compared with those of the UV-Vis spectrum.

In the sonochemical reduction methods, various parameters such as the types of organic additives and dissolved gas, intensity of ultrasound, frequency of ultrasound, and distance between the reaction vessel and the oscillator strongly affect the rates of the reduction of metal ions and properties of the formed metal nanoparticles [7]. If we changed the experimental parameters, the properties of the formed metal nanoparticles would change. However, there are still unclear points regarding the characteristics of the cavitation phenomenon such as the bubble temperatures and pressures, number and size distribution of the bubbles, and its dynamics. If we succeeded in clarifying the cavitation phenomenon in more detail, the sonochemical reduction methods would be promising ones to synthesize various types of novel functional nanoparticles. UV-Vis spectroscopy is expected to be an excellent tool to understand the reduction behavior of metal ions and the formation behavior of metal nanoparticles, as well as a means to understand the characteristics of the cavitation phenomenon.

References

1. Polte J, Ahner TT, Delissen F, Sokolov S, Emmerling F, Thünemann AF, Kraehnert R (2010) Mechanism of gold nanoparticle formation in the classical citrate synthesis method derived from coupled in situ XANES and SAXS evaluation. J Am Chem Soc 132(4):1296–1301
2. Pretzer LA, Nguyen QX, Wong MS (2010) Controlled growth of sub-10 nm gold nanoparticles using carbon monoxide reductant. J Phys Chem C 114(49):21226–21233
3. Pérez-Juste J, Pastoriza-Santos I, Liz-Marzán LM, Mulvaney P (2005) Gold nanorods: synthesis, characterization and applications. Coord Chem Rev 249(17–18):1870–1901
4. Fong Y-Y, Visser BR, Gascooke JR, Cowie BCC, Thomsen L, Metha GF, Buntine MA, Harris HH (2011) Photoreduction kinetics of sodium tetrachloroaurate under synchrotron soft X-ray exposure. Langmuir 27(13):8099–8104
5. Lee YW, Kim M, Han SW (2010) Shaping Pd nanocatalysts through the control of reaction sequence. Chem Commun 46:1535–1537
6. Belloni J (2006) Nucleation, growth and properties of nanoclusters studied by radiation chemistry: application to catalysis. Catalysis Today 113(3–4):141–156
7. Okitsu K (2001) Sonochemical synthesis of metal nanoparticles, chapter 5. In: Pankaj, Ashokkumar M (Eds) Theoretical and experimental sonochemistry involving inorganic systems. Springer, Dordrecht, pp 131–150
8. Anandan S, Ashokkumar M (2011) Sonochemical preparation of monometallic, bimetallic and metal-loaded semiconductor nanoparticles, chapter 6. In: Pankaj, Ashokkumar M (Eds) Theoretical and experimental sonochemistry involving inorganic systems. Springer, Dordrecht, pp 151–169

9. Okitsu K, Iwatani M, Nanzai B, Nishimura R, Maeda Y (2009) Sonochemical reduction of permanganate to manganese dioxide: the effects of H_2O_2 formed in the sonolysis of water on the rates of reduction. Ultrasonics Sonochem 16:387–391

10. Okitsu K, Mizukoshi Y, Bandow H, Maeda Y, Yamamoto T, Nagata Y (1996) Formation of noble metal particles by ultrasonic irradiation. Ultrason Sonochem 3:S249–S251

11. Okitsu K, Yue A, Tanabe S, Matsumoto H, Yobiko Y, Yoo Y (2002) Sonolytic control of rate of gold(III) reduction and size of formed gold nanoparticles: relation between reduction rates and sizes of formed nanoparticles. Bull Chem Soc Jpn 75(10): 2289–2296

12. Okitsu K, Suzuki T, Takenaka N, Bandow H, Nishimura R, Maeda Y (2006) Acoustic multi-bubble cavitation in water: a new aspect of the effect of rare gas atmosphere on bubble temperature and its relevance to sonochemistry. J Phys Chem B 110:20081–20084

13. Tauber A, Mark G, Schuchmann H-P, Von Sonntag C (1999) Sonolysis of tert-butyl alcohol in aqueous solution. J Chem Soc Perkin Trans 2(6):1129–1135

14. Hart EJ, Fischer C-H, Henglein A (1990) Sonolysis of hydrocarbons in aqueous solution. Radiat Phys Chem 36(4):511–516

15. Ashokkumar M, Grieser F (2005) A comparison between multibubble sonoluminescence intensity and the temperature within cavitation bubbles. J Am Chem Soc 127(15): 5326–5327

16. McNamara WB III, Didenko YT, Suslick KS (1999) Sonoluminescence temperatures during multi-bubble cavitation. Nature 401(6755):772–775

17. Didenko YT, McNamara WB III, Suslick KS (1999) Hot spot conditions during cavitation in water. J Am Chem Soc 121(24):5817–5818

18. Hilgenfeldt S, Grossmann S, Lohse D (1999) A simple explanation of light emission in sonoluminescence. Nature 398(6726):402–405

19. Flannigan DJ, Suslick KS (2005) Plasma formation and temperature measurement during single-bubble cavitation. Nature 434(7029):52–55

20. Young FR (1976) Sonoluminescence form water containing dissolved gases. J Acoust Soc Am 60(1):100–104

21. Yasui K (2001) Single-bubble sonoluminescence from noble gases. Phys Rev E Stat Nonlin Soft Matter Phys 63(3II):353011–353014

22. Koda S, Kimura T, Kondo T, Mitome H (2003) A standard method to calibrate sonochemical efficiency of an individual reaction system. Ultrason Sonochem 10(3):149–156

23. Asakura Y, Nishida T, Matsuoka T, Koda S (2008) Effects of ultrasonic frequency and liquid height on sonochemical efficiency of large-scale sonochemical reactors. Ultrason Sonochem 15(3):244–250

24. Beckett MA, Hua I (2001) Impact of ultrasonic frequency on aqueous sonoluminescence and sonochemistry. J Phys Chem A 105(15):3796–3802

25. Hung H-M, Hoffmann MR (1999) Kinetics and mechanism of the sonolytic degradation of chlorinated hydrocarbons: frequency effects. J Phys Chem A 103(15):2734–2739

26. Okitsu K, Ashokkumar M, Grieser F (2005) Sonochemical synthesis of gold nanoparticles: effects of ultrasound frequency. J Phys Chem B 109(44):20673–20675

27. Li Y, Boone E, El-Sayed MA (2002) Size effects of PVP-Pd nanoparticles on the catalytic Suzuki reactions in aqueous solution. Langmuir 18(12):4921–4925

28. Semagina N, Renken A, Laub D, Kiwi-Minsker L (2007) Synthesis of monodispersed palladium nanoparticles to study structure sensitivity of solvent-free selective hydrogenation of 2-methyl-3-butyn-2-ol. J Catal 246(2):308–314

29. Jia C-J, Schüth F (2011) Colloidal metal nanoparticles as a component of designed catalyst. Phys Chem Chem Phys 13(7):2457–2487

30. Okitsu K, Bandow H, Maeda Y, Nagata Y (1996) Sonochemical preparation of ultrafine palladium particles. Chem Mater 8:315–317

31. Creighton JA, Eadon DG (1991) Ultraviolet-visible absorption spectra of the colloidal metallic elements. J Chem Soc Faraday Trans 87(24):3881–3891

32. Okitsu K, Nagaoka S, Tanabe S, Matsumoto H, Mizukoshi Y, Nagata Y (1999) Sonochemical preparation of size-controlled palladium nano-particles on alumina surface. Chem Lett 28:271–272
33. Okitsu K, Yue A, Tanabe S, Matsumoto H (2002) Formation of palladium nanoclusters on Y-zeolite via a sonochemical process and conventional methods. Bull Chem Soc Jpn 75:449–455
34. Wittstock A, Zielasek V, Biener J, Friend CM, Bäumer M (2010) Nanoporous gold catalysts for selective gas-phase oxidative coupling of methanol at low temperature. Science 327(5963):319–322
35. Ma Z, Dai S (2011) Design of novel structured gold nanocatalysts. ACS Catalysis 1(7):805–818
36. Corma A, Garcia H (2008) Supported gold nanoparticles as catalysts for organic reactions. Chem Soc Rev 37:2096–2126
37. Liu C-Y, Tseng W-L (2011) Colorimetric assay for cyanide and cyanogenic glycoside using polysorbate 40-stabilized gold nanoparticles. Chem Commun 47(9):2550–2552
38. Xie J, Zheng Y, Ying JY (2010) Highly selective and ultrasensitive detection of Hg^{2+} based on fluorescence quenching of Au nanoclusters by Hg^{2+}-Au^+ interactions. Chem Commun 46(6):961–963
39. Rodríguez-Lorenzo L, Álvarez-Puebla RA, De Abajo FJG, Liz-Marzán LM (2010) Surface enhanced Raman scattering using star-shaped gold colloidal nanoparticles. J Phys Chem C 114(16):7336–7340
40. Nagata Y, Mizukoshi Y, Okitsu K, Maeda Y (1996) Sonochemical formation of gold particles in aqueous solution. Radiat Res 146:333–338
41. Murphy PJ, LaGrange MS (1998) Raman spectroscopy of gold chloro-hydroxy speciation in fluids at ambient temperature and pressure: a re-evaluation of the effects of pH and chloride concentration. Geochim Cosmochim Acta 62(21–22):3515–3526
42. Haiss W, Thanh NTK, Aveyard J, Fernig DG (2007) Determination of size and concentration of gold nanoparticles from UV-Vis spectra. Anal Chem 79(11):4215–4221
43. Subhramannia M, Pillai VK (2008) Shape-dependent electrocatalytic activity of platinum nanostructures. J Mater Chem 18(48):5858–5870
44. Chen A, Holt-Hindle P (2010) Platinum-based nanostructured materials: synthesis, properties, and applications. Chem Rev 110(6):3767–3804
45. Ratnasamy C, Wagner J (2009) Water gas shift catalysis. Catalysis Rev Sci Engin 51(3):325–440
46. Mizukoshi Y, Oshima R, Maeda Y, Nagata Y (1999) Preparation of platinum nanoparticles by sonochemical reduction of the Pt(II) ion. Langmuir 15(8):2733–2737
47. Mizukoshi Y, Takagi E, Okuno H, Oshima R, Maeda Y, Nagata Y (2001) Preparation of platinum nanoparticles by sonochemical reduction of the Pt(IV) ions: role of surfactants. Ultrason Sonochem 8(1):1–6
48. Stamplecoskie KG, Scaiano JC, Tiwari VS, Anis H (2011) Optimal size of silver nanoparticles for surface-enhanced raman spectroscopy. J Phys Chem C 115(5):1403–1409
49. Shang L, Dong S (2008) Silver nanocluster-based fluorescent sensors for sensitive detection of Cu(II). J Mater Chem 18(39):4636–4640
50. Guo W, Yuan J, Wang E (2009) Oligonucleotide-stabilized Ag nanoclusters as novel fluorescence probes for the highly selective and sensitive detection of the Hg^{2+} ion. Chem Commun 23:3395–3397
51. Nagata Y, Watanabe Y, Fujita S, Dohmaru T, Taniguchi S (1992) Formation of colloidal silver in water by ultrasonic irradiation. J Chem Soc Chem Commun 1992:1620–1622
52. Okitsu K (1993) unpublished result
53. Salkar RA, Jeevanandam P, Aruna ST, Koltypin Y, Gedanken A (1999) The sonochemical preparation of amorphous silver nanoparticles. J Mater Chem 9(6):1333–1335
54. Zhu Y-P, Wang X-K, Guo W-L, Wang J-G, Wang C (2010) Sonochemical synthesis of silver nanorods by reduction of sliver nitrate in aqueous solution. Ultrason Sonochem 17(4):675–679

55. Xu H, Suslick KS (2010) Sonochemical synthesis of highly fluorescent Ag nanoclusters. ACS Nano 4:3209–3214
56. Liu H, Zhang X, Wu X, Jiang L, Burda C, Zhu J-J (2011) Rapid sonochemical synthesis of highly luminescent non-toxic AuNCs and Au@AgNCs and Cu (ii) sensing. Chem Commun 47(14):4237–4239
57. Thackeray MM (1997) Manganese oxides for lithium batteries. Progr Solid State Chem 25(1–2):1–71
58. Zhu S, Zhou H, Hibino M, Honma I, Ichihara M (2005) Synthesis of MnO_2 nanoparticles confined in ordered mesoporous carbon using a sonochemical method. Adv Funct Mater 15(3):381–386
59. Fischer AE, Pettigrew KA, Rolison DR, Stroud RM, Long JW (2007) Incorporation of homogeneous, nanoscale MnO_2 within ultraporous carbon structures via self-limiting electroless deposition: Implications for electrochemical capacitors. Nano Lett 7(2):281–286
60. Dong X, Shen W, Gu J, Xiong L, Zhu Y, Li H, Shi J (2006) MnO_2-embedded-in-mesoporous-carbon-wall structure for use as electrochemical capacitors. J Phys Chem B 110(12):6015–6019
61. Fujimoto T, Mizukoshi Y, Nagata Y, Maeda Y, Oshima R (2001) Sonolytical preparation of various types of metal nanoparticles in aqueous solution. Scr Mater 44(8–9):2183–2186
62. Sostaric JZ, Mulvaney P, Grieser F (1995) Sonochemical dissolution of MnO_2 colloids. J Chem Soc Faraday Trans 91(17):2843–2846
63. Mulvaney P, Cooper R, Grieser F, Meisel D (1990) Kinetics of reductive dissolution of colloidal manganese dioxide. J Phys Chem 94(21):8339–8345
64. Baral S, Lume-Pereira C, Janata E, Henglein A (1985) Chemistry of colloidal manganese dioxide. 2. Reaction with O_2^- and H_2O_2 (pulse radiolysis and stop flow studies). J Phys Chem 89(26):5779–5783
65. Bowman MI (1949) The reaction between potassium permanganate and hydrogen peroxide. J Chem Educ 26(2):103–104
66. Mizukoshi Y, Okitsu K, Maeda Y, Yamamoto TA, Oshima R, Nagata Y (1997) Sonochemical preparation of bimetallic nanoparticles of gold/palladium in aqueous solution. J Phys Chem B 101(36):7033–7037
67. Okitsu K, Murakami M, Tanabe S, Matsumoto H (2000) Catalytic behavior of Au core / Pd shell bimetallic nanoparticles on silica prepared by sonochemical and sol-gel processes. Chem Lett 29(11):1336–1337
68. Mizukoshi Y, Fujimoto T, Nagata Y, Oshima R, Maeda Y (2000) Characterization and catalytic activity of core-shell structured gold/palladium bimetallic nanoparticles synthesized by the sonochemical method. J Phys Chem B 104(25):6028–6032
69. Nakagawa T, Nitani H, Tanabe S, Okitsu K, Seino S, Mizukoshi Y, Yamamoto TA (2005) Structural analysis of sonochemically prepared Au/Pd nanoparticles dispersed in porous silica matrix. Ultrason Sonochem 12(4):249–254
70. Pritchard JC, He O, Ntainjua EN, Piccinini M, Edwards JK, Herzing AA, Carley AF, Moulijn JA, Kiely CJ, Hutchings GJ (2010) The effect of catalyst preparation method on the performance of supported Au–Pd catalysts for the direct synthesis of hydrogen peroxide. Green Chem 12(5):915–921
71. Xu J, White T, Li P, He C, Yu J, Yuan W, Han Y-F (2010) Biphasic Pd-Au alloy catalyst for low-temperature CO oxidation. J Am Chem Soc 132(30):10398–10406
72. Huang X, El-Sayed IH, Qian W, El-Sayed MA (2006) Cancer cell imaging and photothermal therapy in the near-infrared region by using gold nanorods. J Am Chem Soc 128(6):2115–2120
73. Zijlstra P, Chon JWM, Gu M (2009) Five dimensional optical recording mediated by surface plasmons in gold nanorods. Nature 459:410–413

74. Okitsu K, Sharyo K, Nishimura R (2009) One-pot synthesis of gold nanorods by ultrasonic irradiation: the effect of pH on the shape of the gold nanorods and nanoparticles. Langmuir 25(14):7786–7790
75. Jana NR, Gearheart L, Murphy CJ (2001) Wet chemical synthesis of high aspect ratio cylindrical gold nanorods. J Phys Chem B 105(19):4065–4067
76. Nikoobakht B, El-Sayed MA (2003) Preparation and growth mechanism of gold nanorods (NRs) using seed-mediated growth method. Chem Mater 15(10):1957–1962